Journal of Structural Geology, Vol. 13, No. 1, pp. 21 to 35, 1991
Printed in Great Britain

0191-8141/91 $03.00+0.00

Strain factorization and partitioning in the North Mountain thrust sheet, central Appalachians, U.S.A.

MARK A. EVANS*

Department of Geology and Planetary Science, University of Pittsburgh, Pittsburgh, PA 15260, U.S.A.

and

WILLIAM M. DUNNE†

Department of Geology and Geography, West Virginia University, Morgantown, WV 26505, U.S.A.

(*Received* 6 *June* 1989; *accepted in revised form* 28 *May* 1990)

Abstract—By examining finite strain distribution and partitioning strain among deformation mechanisms, a model of thrust sheet deformation is established. The model takes into account kinematic history and environmental conditions.

In the North Mountain thrust sheet of northern Virginia, factorizing finite strain into pure and simple shear components shows that the thrust sheet experienced 6–13% pure shear shortening parallel to the transport direction. Thrust-parallel simple shear strains increase slightly from the top of the thrust sheet toward the base. Within 500 m of the floor thrust, however, simple shear values increase markedly toward the basal thrust. This strain pattern occurs throughout the thrust sheet, overprinting earlier imbricate structures. Therefore, the finite strain in the thrust sheet may be modelled as a transport-parallel pure and simple shear applied during the major transport episode, and after thrust sheet imbrication. This transport-related strain overprints a weak layer-parallel shortening that is probably related to earlier passage of the thrust tip.

Rocks in the thrust sheet with X/Z strain ratios greater than 1.35 have a slight crystallographic preferred orientation and are therefore tectonites in a strict sense. The distribution of tectonites within the thrust sheet defines a 'tectonite front' that is inclined toward the foreland. In the North Mountain thrust sheet the 'tectonite front' also generally coincides with the transition to high-temperature deformation mechanisms, and ultimately may parallel a paleo-isotherm within the thrust wedge.

Strain partitioning indicates that approximately 70% of the finite strain results from intragranular mechanisms (i.e. dislocation glide, dislocation creep and diffusion mechanisms); 25% results from calcite twinning; and less than 5% resulted from transgranular mechanisms such as pressure solution. In non-tectonites, approximately 50% of the finite strain results from pressure solution and intragranular mechanisms, with the remaining strain due to twinning in calcite.

INTRODUCTION

THE variation in the finite strain in the foreland thrust sheet provides insight into its kinematic history. Four deformation events (Fig. 1) are common to the emplacement of many foreland thrust sheets. Layer-parallel shortening preceding or coeval with the passage of the underlying thrust tip is the initial event (Fig. 1a) (Cooper *et al.* 1983, Geiser & Engelder 1983, Williams & Chapman 1983, Marshak & Engelder 1985, Nickelsen 1986, Geiser 1988). Secondly, the thrust sheet is deformed as bending occurs at a ramp hinge during transport. This process results in interlayer slip, non-layer-parallel shortening and bending strains (Fig. 1b) (Wiltschko 1981, Sanderson 1982, Suppe 1983, Wiltschko *et al.* 1985, Kilsdonk & Wiltschko 1988). Thirdly, pure shear shortening and simple shear parallel to the basal thrust (Fig. 1c) accompany thrust sheet transport (Elliott 1976, Mitra & Elliott 1980, Coward & Kim 1981, Fischer & Coward 1982, Sanderson 1982). In some cases, post-emplacement flattening may occur because of passive coupling to underlying footwall rocks that have been shortened by thrust imbrication (Fig. 1d) (Reks & Gray

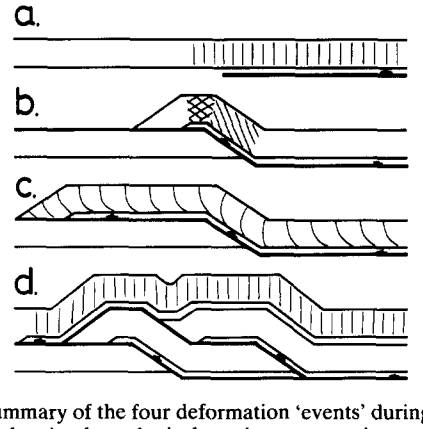

Fig. 1. Summary of the four deformation 'events' during thrust sheet evolution showing hypothetical maximum extension trajectories. (a) Layer-parallel shortening; (b) bending and folding at a ramp hinge; (c) syn-thrusting, transport-related simple shear; and (d) post-emplacement flattening resulting from coupling with an underlying duplex. Short lines represent maximum extension direction and, where crosses, overprinted strains.

*Present address: Department of Geology and Geography, Georgia Southern University, Statesboro, GA 30460-8149, U.S.A.

†Present address: Department of Geological Sciences, University of Tennessee, Knoxville, TN 37996-1410, U.S.A.

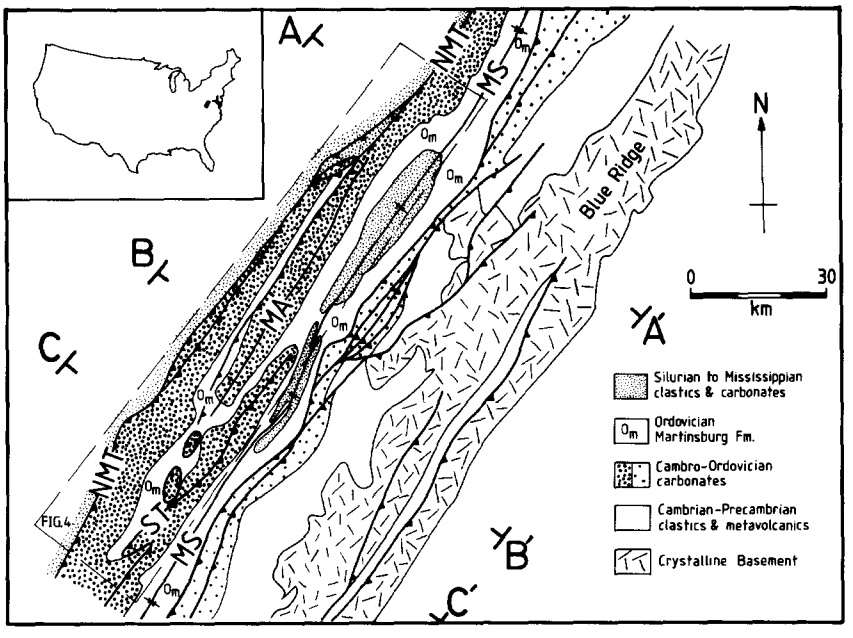

Fig. 2. Location map of study area showing North Mountain thrust sheet (dark stipple) and cross-section locations. Area of Fig. 4 is dashed. MA = Mayland anticline; MS = Massanutten synclinorium; NMT = North Mountain thrust; and ST = Staunton thrust.

1983, Banks & Warburton 1986, Woodward *et al.* 1986, Dunne & Ferrill 1988, Geiser 1988). Although all of these events may contribute to the kinematic history and the finite strain in a foreland thrust sheet, one event may be predominant.

The style of penetrative strain recorded in rocks of a foreland thrust sheet depends on whether intragranular or transgranular deformation mechanisms accommodate the penetrative strain. These mechanisms are controlled by temperature and pressure conditions in the thrust sheet during deformation, and vary both temporally and with structural position in the sheet (Schmid 1982b, Groshong *et al.* 1984a, Groshong 1988). By examining finite strain distributions and causative deformation mechanisms, thrust sheet deformation can be modelled, accounting for kinematic history and environmental conditions.

The purposes of the present study are: (1) to determine, using deformed oolites and calcite twinning, the magnitudes and orientations of finite strains in a foreland carbonate thrust sheet; (2) to partition the finite strain among calcite twinning, other intragranular deformation mechanisms such as dislocation creep and dislocation glide, and transgranular mechanisms such as pressure solution (Groshong *et al.* 1984a); (3) to factorize the finite strain using simple kinematic models to determine the primary deformation event; and (4) to integrate these data to develop a model of penetrative deformation in a large foreland thrust sheet.

GEOLOGICAL SETTING

The large foreland thrust sheet analysed in this study is the North Mountain thrust sheet in northern Virginia, central Appalachians (Evans & Anderson 1986, Evans 1989). The North Mountain thrust (Figs. 2 and 3) extends over 300 km from south-central Pennsylvania to west-central Virginia and marks the sheet's westernmost boundary (Kulander & Dean 1988). The sheet contains an imbricated section of 2000–2300 m thick Cambrian and Ordovician carbonates. Imbricate structures in this sheet formed prior to formation of the Lower North Mountain ramp (LNMR, Fig. 3). The imbricated thrust sheet travelled over the Lower North Mountain ramp and more than 60 km along a flat in the Ordovician Martinsburg Formation, above a correlative carbonate sequence (Evans (1989). After emplacement of the North Mountain thrust sheet, the underlying carbonate section imbricated into a duplex that extends into the western Valley and Ridge province (Evans 1989).

PREVIOUS REGIONAL STRAIN ANALYSES

During his pioneering strain investigations in central Appalachian rocks, Cloos (1947, 1971) utilized ooids in Cambrian and Ordovician carbonates as strain markers. Part of his study area is included in the present investigation. Two reasons for sampling and reinterpreting this area of classic work are: (1) Cloos interpreted his results in terms of a single thick-skinned tectonic event, yet the area is now known to be dominated by thin-skinned thrusting (Harris 1979, Harris *et al.* 1982, Evans & Anderson 1986, Evans 1989); and (2) since Cloos' work (1947, 1971) new strain methods like the R_f/ϕ (Dunnet 1969, Dunnet & Siddans 1972) and Fry (1979) methods have been developed and may be used in combination to partition strain (Ramsay & Huber 1983, 1987).

Other related strain work includes Dean & Kulander's (1972) investigation of oolite deformation near faults in Cambrian and Ordovician carbonates. They found that finite strain markedly increases within

an average of 46 m of thrust and strike-slip faults. Woodward *et al.* (1986) investigated the strain in the Ordovician Martinsburg Formation, the incompetent lithotectonic unit that forms the roof décollement for the North Mountain thrust sheet. Strain magnitudes in the Martinsburg Formation are much larger than those in the North Mountain thrust sheet carbonates, and the orientations of the maximum extension directions are uniformly vertical. Moreover, the strain in the Martinsburg is primarily plane strain with little or no extension parallel to regional strike.

STRAIN ANALYSIS

Finite strain

We collected 72 oriented oolitic limestone samples from different structural positions and stratigraphic levels within the North Mountain thrust sheet (Fig. 4). Three mutually perpendicular thin-sections were cut from each sample and photographed. Depending on the number and quality of the ooids in each thin-section, 50–200 ooid outlines were digitized. Ooid center coordinates, long and short axis orientations, and ellipticities were calculated and used in further analysis.

Two methods of strain determination were used to establish the strain ellipse for each digitized thin-section. R_f/ϕ shape analysis (Dunnet 1969, Dunnet & Siddans 1971, Peach & Lisle 1979, Lisle 1985) was performed for all oolite samples. Fry spatial analysis (Fry 1979, Crespi 1986) was performed for 30 oolite samples in which the oolites are sufficiently anticlustered to produce usable elliptical voids. Results from both the R_f/ϕ and Fry analyses were used to calculate the axial lengths and orientations of a triaxial strain ellipsoid (Gendzwill & Stauffer 1981). Axial lengths for each ellipsoid were recalculated to a normalized constant volume ellipsoid ($XYZ = 1$) (see Appendix 1).

In this study, the two methods generally give the same orientations for principal directions (Fig. 5a). However, strains measured using the R_f/ϕ method are usually about 25% lower than those measured by the Fry method (Fig. 5a). The Fry method yields a value for whole-rock strain being sensitive only to relative particle positions throughout the sample, whereas the R_f/ϕ method measures only particle shape. Homogeneous strains in homogeneous rocks yield the same strain via both methods. The two methods may, however, yield different results where different deformation mechanisms with different efficiencies prevailed in the fine-grained matrix (i.e. diffusion-accommodated grain-boundary sliding) as opposed to the larger grains (i.e. twinning, dislocation glide, fracturing) (Schmid 1982a, Ramsay & Huber 1983, 1987). In those samples with both Fry and R_f/ϕ values, we use the Fry value. The R_f/ϕ values used for the remaining samples should be considered minimum values.

Measured finite strains have X/Z ratios ($X \geq Y \geq Z$) ranging from 1.07 to 3.23 (Appendix 1). The ratios were calculated assuming constant volume deformation. X axes are generally steeply dipping to subvertical, Y axes subparallel to strike and Z axes subhorizontal to moderately inclined toward the hinterland and parallel to the transport direction (Figs. 4, 6a–d and Appendix 1). Axial lengths in the intermediate direction range from 0.90 to 1.10 and average 1.00 ± 0.04 (Appendix 1) indicating that deformation is essentially plane strain. This inference is consistent with the lack of strike-parallel strain determined from incremental strain markers in the overlying Martinsburg Formation (Reks & Gray 1983, Woodward *et al.* 1986).

Twinning strain

We used the calcite strain gauge technique (Groshong 1972, 1974, Groshong *et al.* 1984b) to calculate twinning strains in 25–30 calcite grains from each of two mutually perpendicular thin-sections from 19 of our samples (Fig. 4 and Appendix 2). As outlined in Groshong (1974) and

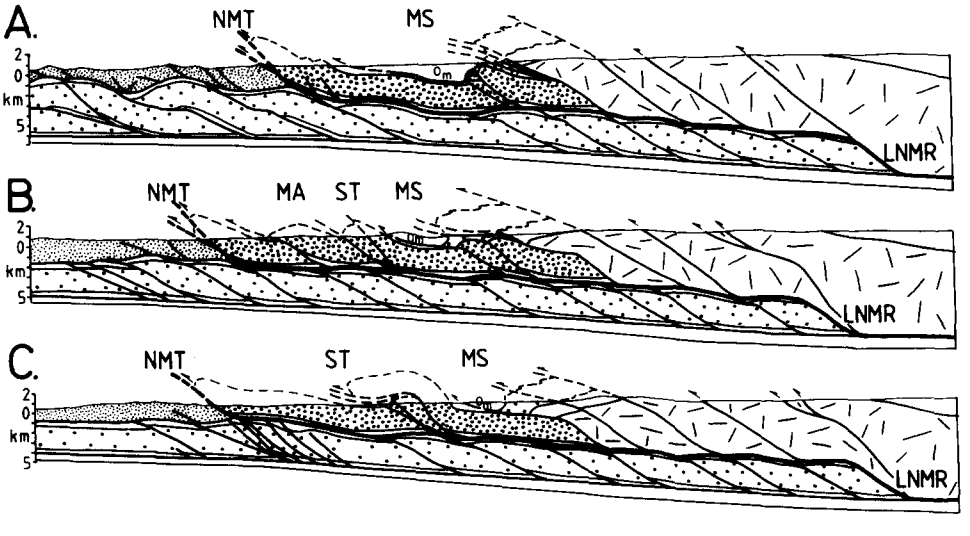

Fig. 3. Cross-sections across the study area. Locations shown in Fig. 2. LNMR = Lower North Mountain ramp, other abbreviations and ornament same as Fig. 2.

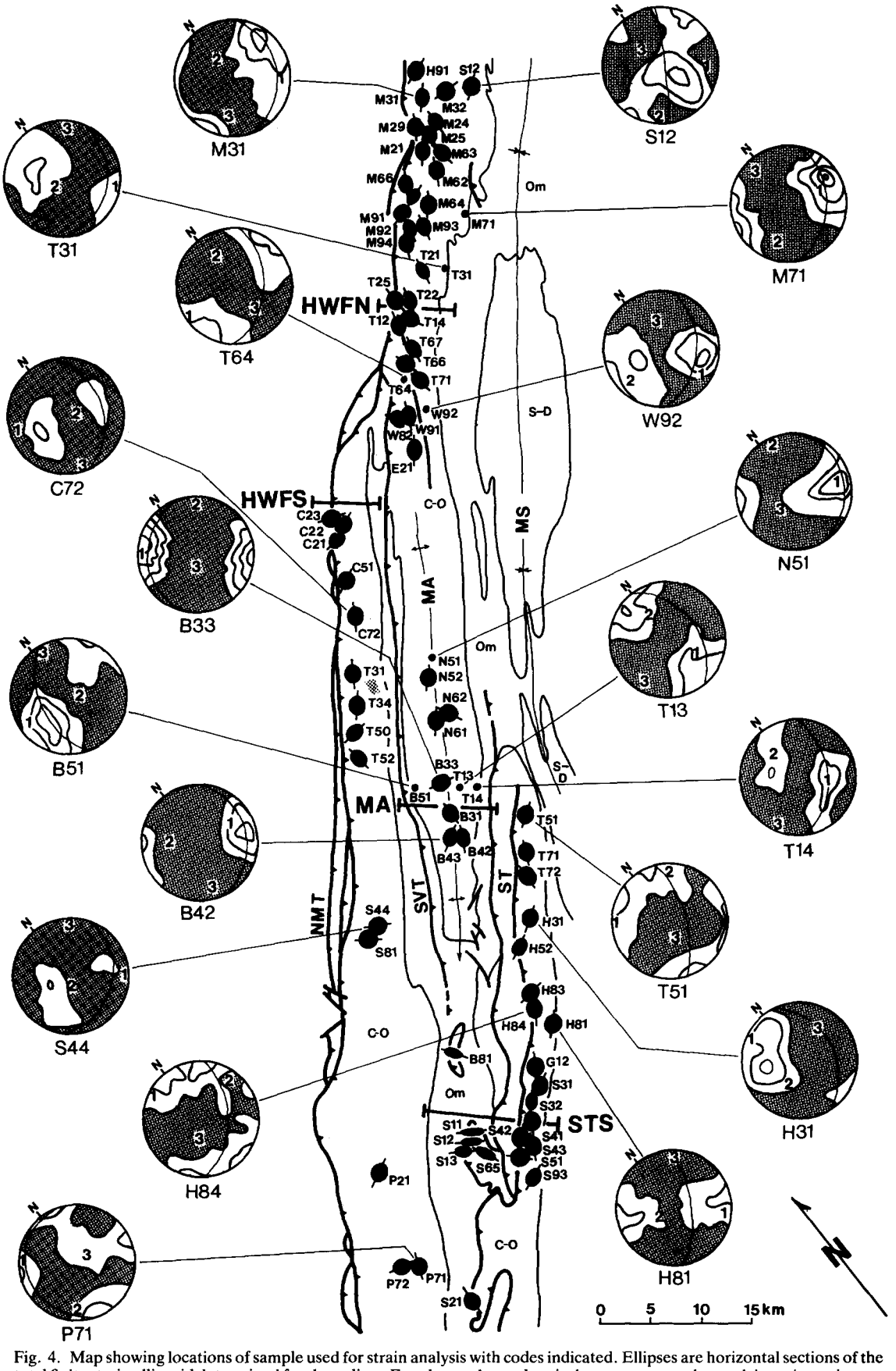

Fig. 4. Map showing locations of sample used for strain analysis with codes indicated. Ellipses are horizontal sections of the total finite strain ellipsoid determined for the oolites. Equal-area, lower-hemisphere stereonets show calcite twin strain axes and contoured Turner (1953) compression axes. The plane of projection for all plots is horizontal. 1 = Maximum shortening direction; 2 = intermediate strain direction; 3 = direction of maximum elongation. The solid great circle indicates the orientation of bedding. Compression axes contours are in multiples of standard deviation starting at 3σ and incremented by 2σ according to the method of Kamb (1959). Locations of cross-sections D–D′ to G–G′ are also shown. MA = Mayland anticline; MS = Massanutten synclinorium; NMT = North Mountain thrust; OR = oblique ramp (Evans 1989); SVT = Saumville thrust; ST = Staunton thrust. Lithology abbreviations are S–D = Silurian through Devonian; Om = Ordovician Martinsburg Formation; C–O = Cambrian and Ordovician carbonates.

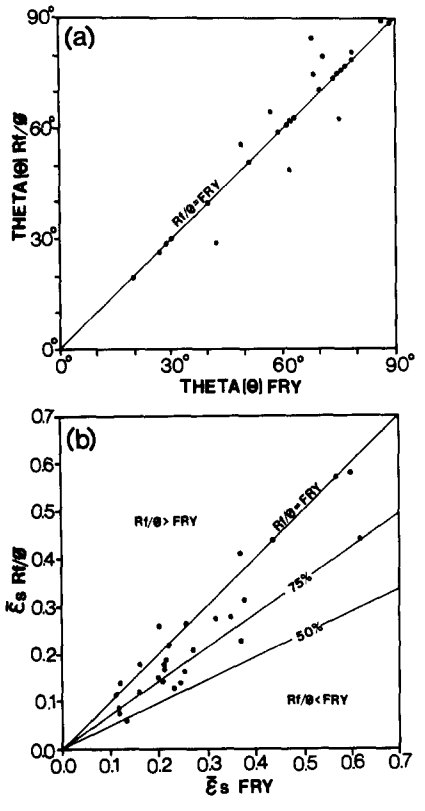

Fig. 5. (a) Plot of θ (angle between profile ellipse long axis and bedding) determined by the R_f/ϕ method vs that by the Fry method. Note that most values fall near the R_f/ϕ = Fry line. (b) Plot of finite strain (ε_s—Nadai 1963) as determined by the R_f/ϕ method vs that by the Fry method. Lines represent percentage of Fry value determined by the R_f/ϕ method.

Groshong *et al.* (1984b), we discarded 20% of our measurements with the largest deviations to 'clean' each sample.

X/Z ratios for the twinning strains range from 1.02 to 1.19 with an average of 1.07 ± 0.04. For the 11 samples with both calcite twinning strain and finite strain measurements, the X/Z ratios for the twinning strains average 1.07 ± 0.05, approximately 26% of the average finite strain ratio of 1.22 ± 0.13. The axes of the calcite twin strain ellipsoids are generally subparallel to the total finite strain axes (Figs. 4, 6a–d and Appendix 2). As with oolite shapes, intermediate axial lengths are approximately 1.00 (Appendix 2) and subparallel to strike, indicating plane strain.

Contoured compression axes (Turner 1953) generally cluster at a single point maxima, however, several samples have polymodal distributions suggesting non-coaxial deformation history (Fig. 4). Three of the 19 samples have negative expected values, a measure of strain inhomogeneity (Groshong 1972), of over 30%, implying multiple deformations or inhomogeneous deformation (Appendix 2).

STRAIN FACTORIZATION

In order to determine which deformation event made the greatest contribution to the finite strain, four simple kinematic models related to the straining 'events' in Fig. 1 may be compared with the strain data. All models are applied assuming plane strain.

From inspection of the strain data, two single event deformation models may be eliminated from consider-

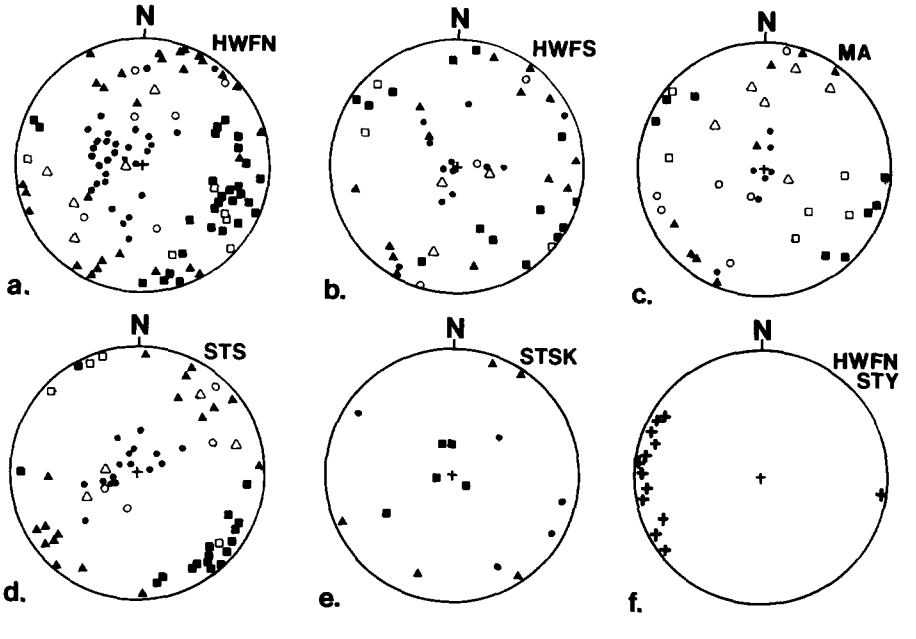

Fig. 6. Equal-area, lower-hemisphere stereonets with ellipsoid axes for each area discussed in text. (a) North Mountain thrust sheet hangingwall flat north of the oblique ramp along the North Mountain thrust (Fig. 4). (b) North Mountain thrust sheet hangingwall flat south of the oblique ramp (Fig. 4). (c) Mayland anticline. (d) Staunton thrust sheet. (e) Staunton thrust sheet klippe rocks. Solid circles are maximum extension axes, solid triangles are intermediate strain axes, and solid squares are maximum shortening axes. Open symbols same as above but for calcite twinning strains. (f) Poles to stylolites (crosses) rotated to bedding horizontal. From North Mountain thrust sheet flat north of the oblique ramp.

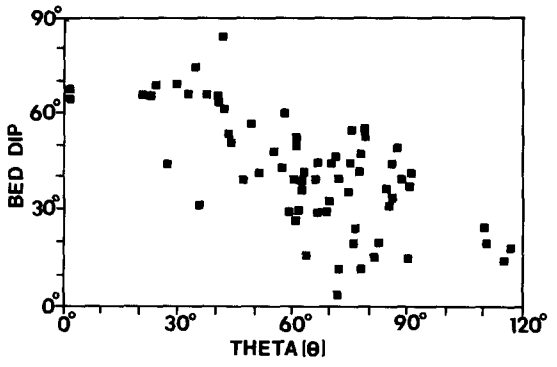

Fig. 7. Plot of bed dip vs θ (angle between profile ellipse long axis and bedding) for all finite strain data used in study.

ation as predominant processes. Layer-parallel shortening did not occur singly because the long axes of the strain ellipsoids are not at a uniform angle to layering (Fig. 7). Because the long axes of the strain ellipsoids are not all vertical (Figs. 6a–d), late flattening is not the only deformation event.

All rocks in the North Mountain thrust sheet have passed across at least one ramp hinge (Evans 1989) (Fig. 3). Abundant bed-parallel slip zones throughout the thrust sheet indicate interbed shear. The zones are commonly infilled with coarsely crystalline to fibrous calcite, but some also contain intensely cleaved mudstone or gouge. Spacing of slip zones varies with bed thickness and ranges from less than 10 cm to more than 2 m. If these slip surfaces were active during the passage of the thrust sheet across the ramp hinges, the maximum bending strain can be estimated using equation (5) in Wiltschko *et al.* (1985). By assuming an average layer thickness of 1 m, an average initial ramp angle of 20–30° (Evans 1989), and an average ramp hinge arc length of 4000–5000 m (Fig. 3), the bending strain is 0.01–0.02% at each hinge. This strain is insignificant and virtually immeasurable. The same conclusion was reached by Wiltschko *et al.* (1985) for a similar section of Cambrian and Ordovician carbonates in the southern Appalachians. Kilsdonk & Wiltschko (1988) suggested that the lack of bending strain is the result of an early strain hardening of the rocks by layer-parallel shortening prior to passage across the ramp.

The North Mountain thrust sheet has travelled at least 60 km along the North Mountain thrust flat (Evans 1989). During transport, a moving thrust sheet may be subject to pure shortening and simple shear components operating parallel to the basal thrust (Coward & Kim 1981, Fischer & Coward 1982, Sanderson 1982). Assuming plane strain, the resulting strain may be factorized into pure and simple shear components. These components are derived from the strain ratio (R) determined for a vertical plane parallel to the bedding dip direction and the angle (θ) of the long (X) axis with bedding (Fig. 8). Because the long and short axes of the strain ellipsoid are not always in the plane of the bedding dip (Figs. 6a–d), R is always less than or equal to the X/Z ratio.

The simple shear component (γ) and the pure shear component, or stretch, (α) may be determined by rewriting Sanderson's (1982) equations (7a) and (7b) to solve for γ and α,

$$\gamma = (R^2 - 1)/(\cot\theta + R^2 \tan\theta) \quad (1)$$

$$\alpha = [(2\gamma)/(\tan 2\theta) - \gamma^2 + 1]^{1/4}. \quad (2)$$

For thrust sheets whose upper boundary is the Earth's surface, $\gamma = 0$ at the top of the sheet increases downward due to drag in the thrust plane (Sanderson 1982).

In strain factorization, a sequence of strain superposition must also be assumed. Since there are no incremental strain markers in the study area to define such a sequence, we choose a sequence of pure shear shortening followed by simple shear for this model. This is done simply for mathematical convenience and does not imply a specific strain history.

REGIONAL STRAIN PATTERNS

Data from the strain analyses are plotted on four cross-sections across the study area (Figs. 9–12). Each cross-section focuses upon a specific structure within the North Mountain thrust sheet. Two sections are from the hangingwall flat portion (HWF) of the thrust sheet, HWFN (Fig. 9) is located north of an oblique ramp in the North Mountain thrust (Fig. 4) (Evans 1989) and HWFS (Fig. 10) lies south of the oblique ramp. A cross-section of the Mayland anticline (MA) (Fig. 11) traverses a ramp anticline within the thrust sheet. The Staunton thrust sheet (STS), an imbricate sheet within the North Mountain thrust sheet, is portrayed in Fig. 12.

Hangingwall flat north cross-section (HWFN)

HWFN (Fig. 9) transects the North Mountain thrust sheet at its westernmost extent where it is least deformed by internal thrusting. Here, the entire thrust sheet thickness is exposed against a footwall ramp from the floor thrust in the Ordovician Martinsburg Formation to the Middle Paleozoic section (NMT, Figs. 3 and 9) (Evans 1989).

From the top of the preserved thrust sheet to approximately 500 m above the floor thrust, finite strain has an average R of 1.30 ± 0.12, although magnitude generally increases toward the floor thrust (Fig. 13). θ averages 70° ± 15° throughout the upper portion of the sheet at

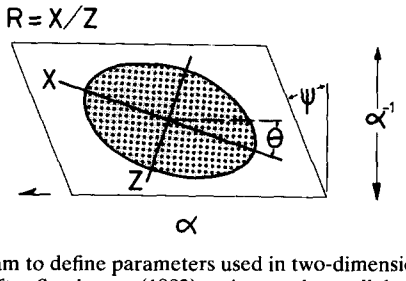

Fig. 8. Diagram to define parameters used in two-dimensional thrust sheet model after Sanderson (1982). α is stretch parallel to the basal thrust, ψ is angular shear, θ is the angle between the ellipse long axis and bedding, and X/Z is the strain ellipse ratio (R).

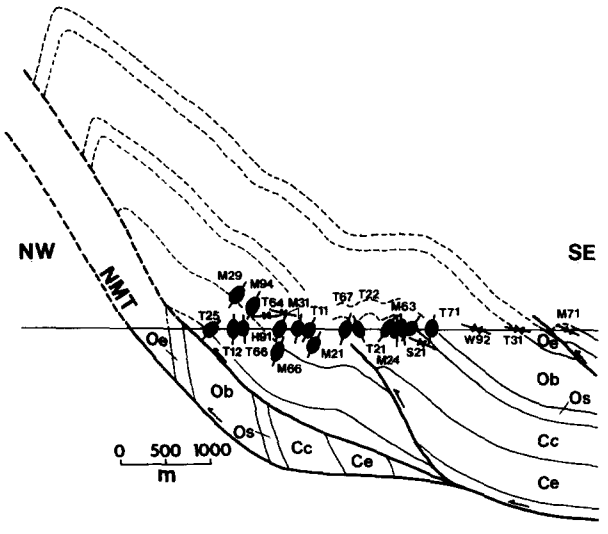

Fig. 9. Cross-section HWFN across the North Mountain thrust sheet hangingwall flat. See Fig. 4 for location. Strain in vertical plane of cross-section is shown with ellipses. Double arrows are the maximum shortening axes determined from the calcite twins with minimum of per cent shortening shown. NMT = North Mountain thrust. Oe = Ordovician Edinburg Formation; Ob = Ordovician Beekmantown Formation; Os = Ordovician Stonehenge Formation; Cc = Cambrian Conococheague Formation; Ce = Cambrian Elbrook Formation; Cw = Cambrian Waynesboro Formation.

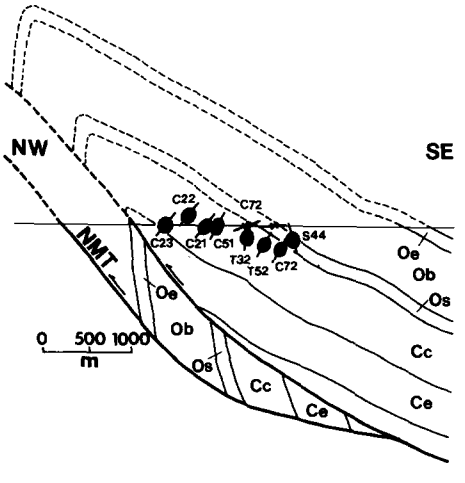

Fig. 10. Cross-section HWFS across the North Mountain thrust sheet flat. See Fig. 4 for location. Symbols and abbreviations same as Fig. 9.

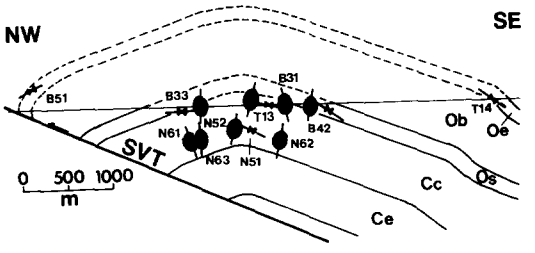

Fig. 11. Cross-section MA across the Mayland anticline. See Fig. 4 for location. Symbols and abbreviations same as in Fig. 9.

this location (Figs. 9 and 13) with no systematic variation with proximity to the floor thrust. Locally, finite strains are complicated by the formation of secondary folds and imbricate thrusts (Fig. 9) (Dean & Kulander 1972). These strain data are not included in this factorization for events affecting the entire sheet.

Factorizing (R,θ) to (α,γ) (Fig. 13, Table 1), the pure shear component (α) averages 9% ± 4% shortening, and the simple shear component (γ) averages 0.13 ± 0.07 (a 7.5° shear angle) with a general increase toward the floor thrust. Within 500 m of the floor thrust, magnitudes of the finite strain increase, R values reach 2.06 with an average of 1.62 ± 0.22; θ angles decrease markedly and average 34° ± 22°. Factorizing these data gives values of up to 8% thrust-parallel extension and a large component of simple shear (Fig. 13 and Table 1).

Study of calcite twins reveals shortening that ranges from 2.2 to 4.8% with an average value of 3.4% ± 0.8% (Appendix 2). Four of the six samples from the HWFN area (M31, M61, T31, W92) have maximum extension axes subperpendicular to bedding (θ is 68–90°), whereas samples S12 and T64 have θ angles of 30°. Sample T64 has 41% negative expected values indicating a non-coaxial strain history, possibly including a large component of bed-parallel simple shear. Sample S12 is from a bed that has a subvertical dip and bed rotation may have complicated the twinning strains. In general, however, the calcite twin strain ellipsoid axes are subparallel to those from the finite strain data. The compression axes generally cluster about a single point maxima, indicating a simple twinning history (Fig. 4). This is supported by a low negative expected value average of 14.2% ± 8.6% for all samples except T64 (Appendix 2).

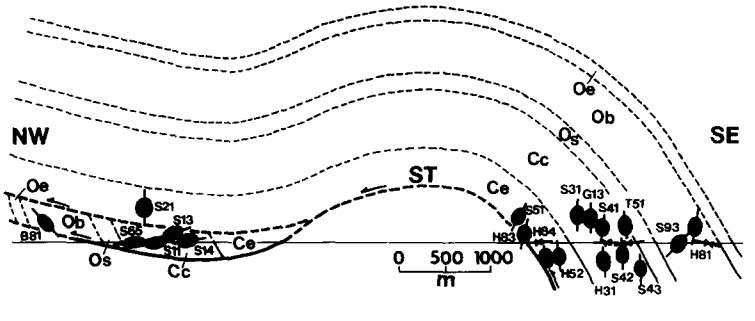

Fig. 12. Cross-section STS across the Staunton thrust sheet and associated klippe. See Fig. 4 for location. Symbols and abbreviations same as in Fig. 9.

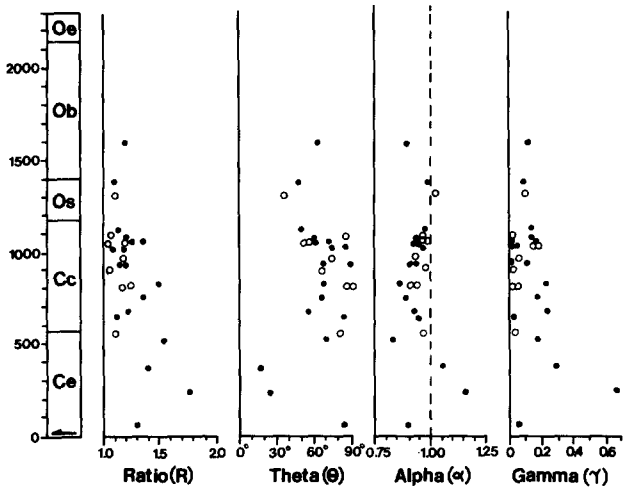

Fig. 13. Summary of strain parameters from the North Mountain thrust sheet hangingwall flat cross-sections (HWFN and HWFS). Solid circles are samples from section HWFN (Fig. 9) and open circles are from section HWFS (Fig. 10). Stratigraphic abbreviations same as in Fig. 10.

Hangingwall flat south cross-section (HWFS)

The HWFS (Figs. 4 and 10) section also cuts the hangingwall flat of the North Mountain thrust sheet and shows similar structural geometry and strain orientations to section HWFN (Fig. 9). The samples in this section are primarily from the central part of the thrust sheet and have an average R of 1.14 ± 0.07 (Appendix 1). The lower 500 m of the thrust sheet is not exposed in this part of the study area. Strain factorization yields an average α of $6\% \pm 0.4\%$ and an average γ of 0.05 ± 0.05 (Fig. 13), which are slightly less than those determined for the HWFN section.

Maximum shortening axes determined from calcite twinning strains are subhorizontal with only 1.5–1.9% shortening (Fig. 10 and Appendix 2). Calcite compression axes for the two samples measured in this section (C72 and S44) have a bimodal distribution that suggests multiple deformations (Fig. 4).

The Mayland anticline (MA) and Staunton thrust sheet cross-sections (STS)

The results from the factorization provide an explanation for strain distribution using a kinematic interpretation of pure and simple shear parallel to thrust transport. With this interpretation in mind, we examine results from the MA and STS cross-sections traversing structures that formed prior to the formation of the North Mountain thrust sheet (Figs. 12 and 13). However, a decision must be made as to how the strains should be factorized. If the strains are factorized with respect to layering, an assumption is that the strain is primarily the result of formation of the imbricate structures. However, if the strains are factorized with respect to the floor thrust, an assumption is that the strain is primarily a result of transport along the North Mountain thrust. Because the orientations of finite strain ellipsoid axes (Figs. 6a–d) are similar for the HWFN, MA and STS structures, the strains in all structures probably resulted from the same deformation event. Therefore, strain factorization for the MA and STS sections is done with respect to the floor thrust. For comparison, results from factorization with respect to bedding are also presented.

The Mayland anticline (Figs. 4 and 11) is an extensive ramp anticline above the Saumsville thrust in the North Mountain sheet. The fold is symmetric with 20° limb dips. At the leading edge of the structure, intensely fractured and veined beds are steeply-dipping to subvertical. Finite strain data indicate a subhorizontal shortening (Figs. 6c and 11) with an average R of 1.34 ± 0.07 (Appendix 1). If the strain is factorized with respect to a subhorizontal floor thrust, the rocks sampled would have been 2000–3000 m above the thrust during major transport. The average γ values (-0.02 ± 0.06) indicate very little simple shear component, whereas the average α values show a considerable and constant ($13\% \pm 2\%$) shortening (Table 1). These results are consistent with a deformation model that predicts a small simple shear component far from the basal thrust. Although if factorization is done with respect to bedding, the results are quite similar (Table 1) reflecting the low bedding dips and constant strain orientation. However, samples B33 and N52 from the northwest limb of the anticline, have negative gamma values that are inconsistent with the thrust-transport model.

Twinning strains range from 1.1 to 6.9% shortening with an average value of $3.4\% \pm 2.0\%$ (Appendix 2). Maximum shortening axes are subhorizontal to gently plunging in the direction of bedding dip (Figs. 4 and 11). This result suggests that twinning may have initiated during an early layer-parallel shortening event, and continued through formation of the Mayland anticline and possibly during thrust sheet transport. This is supported by the moderately high negative expected values averaging $23.3\% \pm 6.6\%$ (Appendix 2). The sample with the highest strain (B51) is from the steep frontal limb of the fold that may have been rotated during thrusting of the anticline. Calcite twin compression axes

Table 1. Results of strain factorization

Factorization		HWFN	HWFS	MA	STS
Layer-parallel	Pure	0.91 ± 0.04	0.94 ± 0.04	0.90 ± 0.04	0.97 ± 0.06
	Simple	0.13 ± 0.07	0.05 ± 0.05	0.05 ± 0.09	0.22 ± 0.14
Thrust-parallel	Pure	0.91 ± 0.04	0.94 ± 0.04	0.87 ± 0.02	0.89 ± 0.05
	Simple	0.13 ± 0.07	0.05 ± 0.05	0.02 ± 0.06	0.09 ± 0.08

generally cluster at a single point maximum which falls near the bedding great circle (Fig. 4), supporting initiation of twinning during early layer-parallel shortening.

The Staunton thrust sheet (Figs. 4 and 12) is a major imbricate sheet within the North Mountain sheet. Displacement along the Staunton thrust increases southwestward along strike from 0 to 9 km in less than 40 km. Cambrian and Ordovician carbonates from the largely eroded overturned northwest limb of the thrust sheet are preserved in klippe (Evans 1989). Klippe rocks are the most intensely deformed of any in the study area. Having a subhorizontal cleavage and maximum extension directions that are subparallel to the thrust and transport direction (Figs. 6e and 12). Oolite strain ratios (R) range from 1.54 to 3.2 (Appendix 1) with an average of 2.20 ± 0.54. These rocks are not considered in the strain factorization because they were exposed to local deformation events.

The following discussion focuses upon the well preserved Staunton thrust sheet flat that is emplaced on the Staunton footwall ramp (Fig. 12). Bed dips in the hangingwall flat have been steepened to more than 45° by imbrication in the footwall. Finite strain magnitudes from the Staunton hangingwall flat shows an average R of 1.31 ± 0.13 (Appendix 1) with a subhorizontal maximum shortening direction (Figs. 4, 6d and 12). Factorizing strain parallel to a floor thrust 3000 m below, the average γ values (-0.09 ± 0.08) indicate very little simple shear component, whereas the average α values show a considerable ($11\% \pm 6\%$) shortening (Table 1). These values are similar to those determined for the HWFN and MA sections. In contrast, if the strain is factorized with respect to bedding, the pure shear component is only 3% and the simple shear component is a very large 0.22 (Table 1). These results are inconsistent with those from the HWFN and MA sections, thereby supporting factorization with respect to the floor thrust.

Calcite twinning strains range from 1.3 to 8.1% shortening with an average of $3.9\% \pm 3.2\%$ (Appendix 2). Maximum shortening axes (Figs. 6d and 12) are generally subhorizontal. This geometry is consistent with deformation parallel to the North Mountain floor thrust rather than layer-parallel deformation. As with the MA section, the average negative expected value is moderately high ($22.8\% \pm 5.6\%$) (Appendix 2), suggesting non-coaxial deformation. Unlike other areas in the North Mountain thrust sheet, however, compression axis distributions are multimodal and show no simple relationship to the maximum shortening axes (Fig. 4).

Although the factorization results suggest a model of pure and simple shear parallel to the floor thrust, the finite strain data do not provide a unique solution. Late flattening, superimposed on earlier strains, as a result of Lower Carbonate duplex imbrication, cannot be ruled out. Because the Lower Carbonate duplex is shortened by 20% by thrust imbrication (Evans 1989), this is also the maximum possible shortening strain that can be attributed to a flattening event. However, the shortening is not evenly distributed in the North Mountain thrust sheet (Figs. 4 and 9–13) as would be expected in a single late-flattening deformation event, suggesting a limited contribution to the finite strain.

STRAIN PARTITIONING AND DEFORMATION MECHANISMS

Strain partitioning

Strain partitioning (Ramsay & Huber 1983, 1987, Groshong *et al.* 1984a) is an effort to separate the finite strain into components caused by different deformation mechanisms. Following Groshong *et al.* (1984a), an attempt has been made to partition the finite strain into: (1) transgranular strains (stylolites) resulting from grain to grain pressure solution in an aqueous environment; (2) intragranular strains resulting from intracrystalline glide, dislocation creep, lattice and grain-boundary diffusion, and diffusion-accommodated grain-boundary sliding; and (3) twinning strain. Twinning is singled out from other intragranular mechanisms because it is operative under low temperature and pressure conditions, and is easy to measure optically. Several deformation mechanisms may be active simultaneously. As strain and/or strain rates change, or environmental conditions change, some mechanisms may cease to function and others become prominent (Groshong *et al.* 1984a). Groshong (1988) grouped deformation mechanisms into associations related to deformation intensity that are recognizable in the North Mountain thrust sheet.

The least deformed rocks fall into the semi-brittle framework deformation association III (Groshong 1988) characterized by: (1) a general lack of preferred crystallographic orientation; (2) abundant calcite twinning; (3) rare bent twins and undulatory extinction indicating glide along lattice planes; (4) uncommon, thin-section scale pressure solution recognized as discontinuous stylolites between micrite clasts, ooids and spar; and (5) rare mesoscale pressure solution recognized as bed-perpendicular stylolites. These rocks occur in the structurally highest parts of the thrust sheet, >800 m above the floor thrust in the HWFS section; >1100 m from the floor thrust in the HWFN section; and >2500 m from the floor thrust in the MA section (Appendix 1). Association III rocks are not found in the STS section.

The mesoscale bed-perpendicular stylolites provide evidence for an early layer-parallel shortening event with a dominant E–W shortening (Fig. 6f). The thin-section scale stylolites, however, are perpendicular to the maximum shortening direction determined from the finite strain data (N60°W). Calcite twinning accounts for approximately 2.5% shortening, which is over half of the finite strain in rocks of association III; shortening by pressure solution on the thin-section scale is estimated to be 1–3%; and shortening by mesoscopic pressure solution is estimated to be <1% (Fig. 14). The amount of shortening due to pressure solution was estimated by determining the average stylolite spacing and amount of material lost at each stylolite.

Rocks in the lower portion of the thrust sheet, near imbricate thrusts, in fold hinges, and in overturned fold limbs may contain structures characteristic of association IV—glide (IVG) and recrystallization (IVR) tectonites, Groshong (1988). These rocks are characterized by: (1) preferred crystallographic orientation; (2) extensive calcite twinning; (3) abundant bent twins and undulatory extinction; (4) recrystallization evidenced by core and mantle structures, subgrain formation, twin-boundary migration and serrate grain boundaries suggesting grain-boundary migration; and (5) pressure solution recognized by uncommon, thin-section scale stylolites. Rocks in association IVG have original grain boundaries preserved, whereas rocks in association IVR have no original grain boundaries preserved (Groshong 1988).

Rocks of both associations (IVG and IVR occur within 1100 m of the floor thrust in the HWFN section; within 800 m of the floor thrust in the HWFS section; within 2500 m of the floor thrust in the MA section; and throughout the STS section (Appendix 1). Within 500 m from the floor thrust in the HWFN section the rocks are primarily association IVR (Appendix 1).

We denote tectonites with <50% recrystallized grains as association IVG (Appendix 1). In associations IVG, IVG+ and IVR, intragranular mechanisms account for over 70% of the finite strain; twinning about 25% of the finite strain; and pressure solution <7% of the finite strain (Fig. 14).

The boundary between associations III and IV is the 'tectonite front' (Groshong 1988) and is defined by the

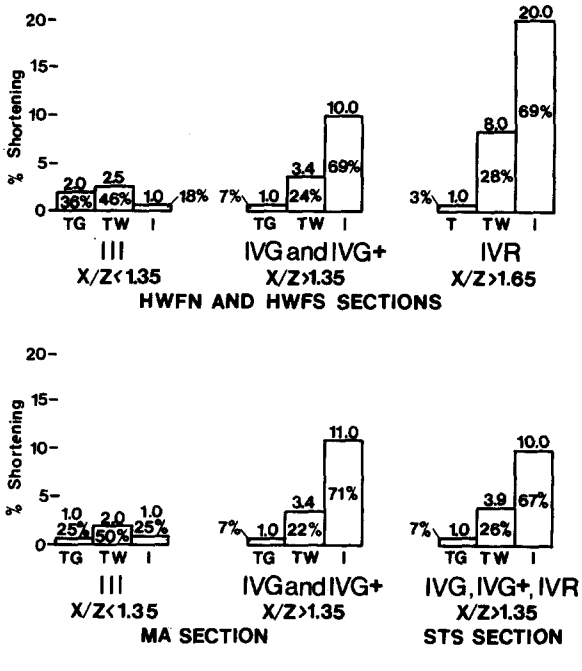

Fig. 14. Summary of strain partitioning data. Deformation associations III, IVG, IVG+ and IVR are as defined in text. TG is transgranular deformation mechanisms including pressure solution. TW is calcite twinning. I is intragranular deformation mechanisms excluding twinning (after Groshong *et al.* 1984a). X/Z is strain ratio of finite strain ellipsoid long and short axes. Values in graph are percentage of total strain attributed to that particular group of deformation mechanisms. Values shown above graph are in % shortening attributed to that particular group of deformation mechanisms.

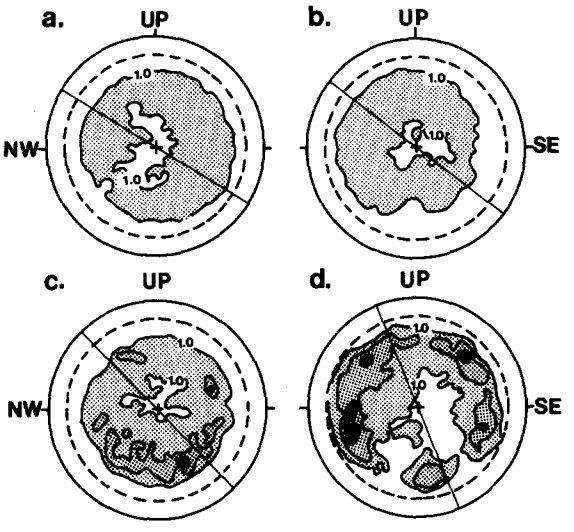

Fig. 15. Pole-figures for *r* glide twinning plane (1011) (Bravais indices) determined by X-ray texture analysis for four limestone samples from various structural levels within the North Mountain thrust sheet. (a) Sample T31 ($X/Z = 1.05$) is from near the top of the thrust sheet. (b) Sample M62 ($X/Z = 1.14$), from 1100 m above the floor thrust. Both have no preferred crystallographic orientation. (c) Sample H91 ($X/Z = 1.43$) is from about 800 m above the floor thrust and has a slight preferred orientation. (d) Sample T12 ($X/Z = 2.05$ is from 200 m above the floor thrust and has a strong preferred orientation. Contour interval is 0.2 mean random distribution. Projections are equal-angle in a vertical plane parallel to the transport direction. Bedding dip for each sample is shown.

appearance of a preferred crystallographic orientation in association IV. Although these associations have not been previously applied to the study area, Cloos (1947, 1971) defined a 'tectonite front' from oolite X/Z ratios to the east of the study area, between the Massanutten synclinorium and the Blue Ridge (Fig. 2). Mitra (1987), on the other hand, classified all rocks in the North Mountain thrust sheet as tectonites by placing a 'carbonate tectonite front' at the North Mountain thrust outcrop (Fig. 2). However, recognition of the occurrence of a preferred crystallographic orientation would more rigorously define the front location. Examining the X-ray texture pole figures for the calcite *r* twin plane (1011) (Bravais indices), sample T31 ($X/Z = 1.05$) (Fig. 15a), from near the top of the thrust sheet, and sample M62 ($X/Z = 1.14$) (Fig. 15b), from 1100 m above the floor thrust, have no preferred crystallographic orientation; sample H91 ($X/Z = 1.45$) (Fig. 15c), from about 800 m above the floor thrust, has a slight preferred orientation; and sample T12 ($X/Z = 2.05$) (Fig. 15d), from 200 m above the floor thrust, has a strong preferred orientation. These data indicate that a 'tectonite front', as defined by Groshong (1988), may be placed within the North Mountain thrust sheet where X/Z ratios exceed approximately 1.35.

Deformation mechanism maps

Temperature is the primary controlling factor for determining operative deformation mechanisms (Groshong 1988). The maximum temperature to which rocks have been subjected in the North Mountain thrust sheet may be interpreted from conodont color alteration

(Epstein *et al.* 1977). Conodont alteration indices in the Cambrian and Ordovician carbonates range from 4.5 to greater than 5.5 (Epstein *et al.* 1977, Harris *et al.* 1978, Rejebian *et al.* 1987) indicating a temperature range of 250°C to at least 350°C, and possibly as high as 400°C. Deformation mechanism maps for calcite in this temperature range (Fig. 16) suggests mechanisms that were probably active during the deformation of the North Mountain thrust sheet. At the lower temperature limit (250°C) and at geologic strain rates in thrust systems (10^{-13}–10^{-15} s^{-1}) (Pfiffner & Ramsay 1982) twinning and other glide mechanisms, are active in grains of 5 μm and larger. Smaller grains are deformed by diffusion mass transfer. At the upper temperature limit (350°C), diffusion mass transfer is the dominant mechanism for grains smaller than 50 μm, but high-temperature power-law mechanisms, including recrystallization, occur in larger grains.

By comparing the deformation mechanisms that were operative in the rocks at a given grain size with temperature-dependent mechanism maps, the temperature of deformation may be estimated. However, each field of a deformation mechanism map only indicates which mechanisms are dominant under certain grain size and pressure conditions. Mechanisms from neighboring fields may also be active, but to a lesser degree (Freeman & Ferguson 1986). Therefore, samples in association IVG+ may indicate the transition to high-temperature deformation mechanisms (at approximately 350°C) by an increased presence of recrystallized grains.

Increased recrystallization results in strain softening by grain size reduction, and ultimately larger strains resulting from increased strain rates assuming constant stress (Schmid 1982b). Rocks with these large strains are generally association IVR rocks, and are found near thrust faults, in fold hinges and in overturned fold limbs.

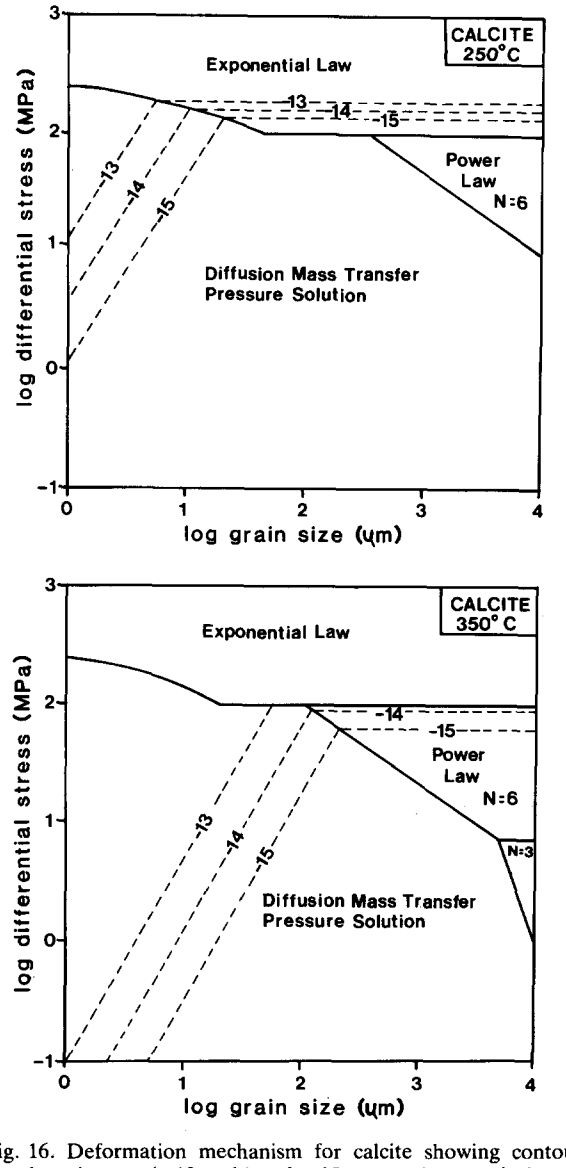

Fig. 16. Deformation mechanism for calcite showing contours of equal strain rate (−13, −14 and −15 are strain rates in $\log_{10}$ s^{-1}). (a) 250°C. (b) 350°C. Calculated from flow laws given by Rutter (1974, 1976) and Schmid *et al.* (1977, 1980, 1982a).

DEFORMATION MODEL

The four structural cross-sections (Figs. 9–12) can be integrated to show the distribution of finite strain and deformation mechanisms in a schematic foreland thrust sheet (Fig. 17a). The factorization results are best modelled as strain accumulated during major transport of the North Mountain thrust sheet. Finite strain and simple shear increase from the top of the thrust sheet toward the base as a result of an increasing continuous shear response toward the sheet bottom (Fig. 17b).

A 'tectonite front', which separates rocks in association III from those in associations IVG, IVG+ and IVR, is shown in Figs. 17(a) & (b). Many tectonite samples are partly recrystallized (association IVG+, see Appendix 1 and 2), indicating that the front corresponds to the transition from low-temperature to high-temperature deformation.

The transition zone between dominantly high-temperature and dominantly low-temperature deformation (about 350°C) may be used to establish a paleo-isotherm within the thrust wedge. However, several assumptions are required. Firstly, the strain and deformation mechanisms must be a result of a single deformation event. In the case of the North Mountain thrust sheet this event is transport of the thrust sheet. Secondly, the experimentally determined deformation mechanism maps must accurately show the mechanism boundaries.

If the overburden is the primary source of heat within the thrust wedge, the 'tectonite front' may reflect the geometry of the wedge surface. Depending upon the geothermal gradient in the thrust system (Suppe & Wittke 1977, Tissot & Welte 1978, Nathenson & Guffanti 1988), an overburden of 6.5 km (50°C km^{-1}) to 13 km (25°C km^{-1}) is needed to increase the temperature to 350°C. As shown in Fig. 17(c), the regional slope of the foreland-dipping overburden surface would result in a critical taper angle of approximately 8°. This angle falls within the critical taper angles for thrust wedges (Davis *et al.* 1983).

However, Barr & Dahlen (1989) have determined

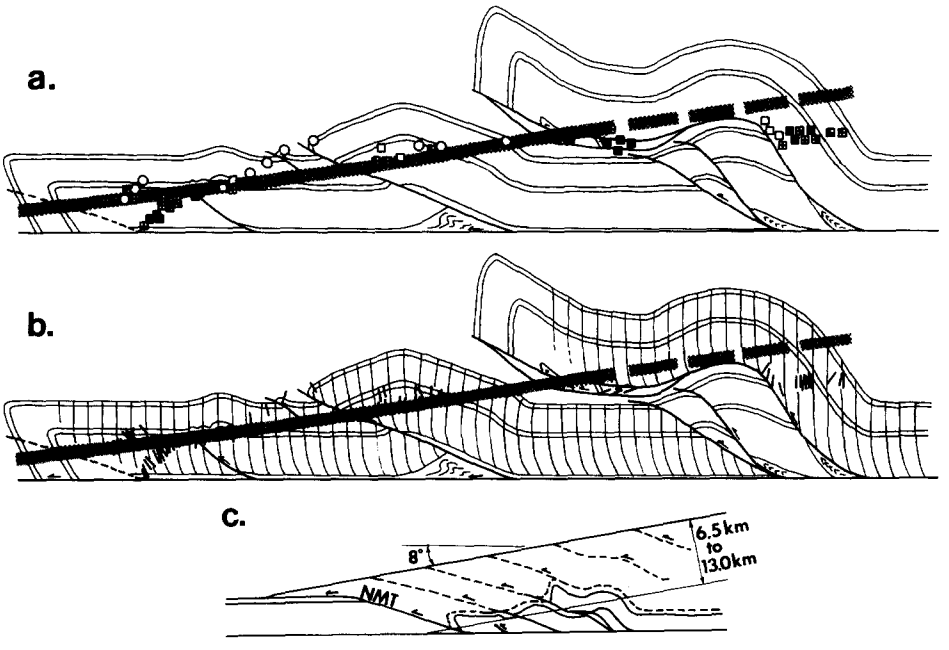

Fig. 17. (a) Schematic cross-section integrating the structural components of the North Mountain thrust sheet. Shown are positions of finite strain data and their deformation mechanism associations: open circle—association III; open square—association IVG; square with cross—association IVG+; solid square—association IVR. Shaded line indicates approximate tectonite front and boundary between high- and low-temperature deformation regimes. (b) Same as above but showing spatial relationships of the strain data used in the study, and interpreted maximum extension trajectories. Trajectories not shown where there is a lack of strain data such as in smaller imbricate thrust sheets and leading edge folds. (c) Schematic cross-section showing interpreted thrust wedge geometry based on location of tectonite front and occurrence of calcite recrystallization.

that strain and shear heating, as well as the effects of erosion and accretion, are important contributors to the total heat budget within the thrust wedge. Isotherms within the wedge are generally more steeply dipping toward the foreland than the erosion surface (see Barr & Dahlen 1989, figs. 5 and 25). Therefore, the orientation of the tectonite front may only provide an estimate of the maximum taper angle (Fig. 17c).

CONCLUSIONS

(1) The finite strain in the North Mountain thrust sheet may most simply be modelled as transport-related thrust-parallel pure and simple shear applied after thrust sheet imbrication. This strain overprints a low-magnitude early layer-parallel shortening that is probably related to passage of the thrust tip.

(2) Rocks with an X/Z strain ratio of >1.35 are classified as tectonites. The distribution of these rocks within the thrust sheet defines a 'tectonite front' that is inclined toward the foreland. In the North Mountain thrust sheet this 'tectonite front' also approximately defines the transition to high-temperature deformation mechanisms, and ultimately may reflect the 350°C isotherm within the thrust wedge.

(3) In the tectonites, strain partitioning indicates that approximately 70% of the finite strain is a result of intragranular mechanisms (i.e. dislocation glide, dislocation creep and diffusion-accommodated grain-boundary sliding); 25% results from calcite twinning; and $<5\%$ can be attributed to transgranular mechanisms such as pressure solution. In non-tectonites, approximately 50% of the finite strain results from calcite twinning, and the remaining 50% from pressure solution and intragranular mechanisms.

Acknowledgements—We are grateful to Norman Gray for providing digitizing programs, and to Brian Gendzwill for the triaxial ellipsoid analysis program. William Hu and John Butler deserve thanks for their assistance and co-operation in the X-ray texture analysis. Critical readings of various versions of this paper by Thomas Anderson, David Ferrill, Richard Groshong, Charles Onasch, David Sanderson and Steven Wojtal helped to improve the manuscript. Funding was provided by National Science Foundation grant EAR-8520629, the Appalachian Basin Industrial Associates, and a Geological Society of America grant to Mark Evans.

REFERENCES

Banks, C. J. & Warburton, J. 1986. 'Passive-roof' duplex geometry in the frontal structures of the Kirthar and Sulaiman mountain belts, Pakistan. *J. Struct. Geol.* **8**, 229–237.

Barr, T. D. & Dahlen, F. A. 1989. Brittle frictional mountain building, 2. Thermal structure and heat budget. *J. geophys. Res.* **94**, 3923–3940.

Cloos, E. 1947. Oolite deformation in the South Mountain fold, Maryland. *Bull. geol. Soc. Am.* **58**, 843–918.

Cloos, E. 1971. *Microstructures along the Western Edge of the Blue Ridge, Maryland and Virginia. Studies in Geology* 20. Johns Hopkins University Press, Baltimore.

Cooper, M. A., Garton, M. R. & Hossack, J. R. 1983. The origin of the Basse Normandie duplex, Boulonnais, France. *J. Struct. Geol.* **5**, 139–152.

Coward, M. P. & Kim, J. H. 1981. Strain within thrust sheets. In: *Thrust and Nappe Tectonics* (edited by McClay, K. R. & Price, N. J.). *Spec. Publs. geol. Soc. Lond.* **9**, 275–292.

Crespi, J. M. 1986. Some guidelines for the practical application of Fry's method of strain analysis. *J. Struct. Geol.* **8**, 799–808.

Davis, D., Suppe, J. & Dahlen, F. A. 1983. Mechanics of fold-thrust belts and accretionary wedges. *J. geophys. Res.* **88**, 1153–1172.

Dean, S. L. & Kulander, B. R. 1972. Oolite deformation associated with faulting in the northern Shenandoah Valley. In: *Appalachian Structures: Origin, Evolution, and Possible Potential for New Exploraton Frontiers* (edited by Lessing, P., Hayhurst, R. I., Barlow, J. A. & Woodfork, L. D.). West Virginia geol. Survey, 72–90.

Dunne, W. M. & Ferrill, D. A. 1988. Blind thrust systems. *Geology* **16**, 33–36.

Dunnet, D. 1969. A technique of finite strain analysis using elliptical particles. *Tectonophysics* **7**, 117–136.

Dunnet, D. & Siddans, A. W. B. 1971. Non-random sedimentary fabrics and their modification by strain. *Tectonophysics* **12**, 307–325.

Elliott, D. 1976. The energy balance and deformation of thrust sheets. *Phil. Trans. R. Soc. Lond.* **A283**, 289–312.

Epstein, A. G., Epstein, J. B. & Harris, L. D. 1977. Conodont color alteration—an index to organic metamorphism. *Prof. Pap. U.S. geol. Surv.* **995**.

Evans, M. A. 1988. Vertical strain variation in a thrust sheet: An example from the North Mountain thrust sheet, Virginia. *Geol. Soc. Am. Abs. w. Prog.* **20**, 263.

Evans, M. A. 1989. The structural geometry and evolution of foreland thrust systems, northern Virginia. *Bull. geol. Soc. Am.* **101**, 339–354.

Evans, M. A. & Anderson, T. A. 1986. The structural geometry of the North Mountain duplex, northwestern Virginia. *Geol. Soc. Am. Abs. w. Prog.* **18**, 596.

Fischer, M. W. & Coward, M. P. 1982. Strains and folds within thrust sheets: an analysis of the Heilam sheet, northwest Scotland. *Tectonophysics* **88**, 291–312.

Freeman, B. & Ferguson, C. C. 1986. Deformation mechanism maps and micromechanics of rocks with distributed grain sizes. *J. geophys. Res.* **91**, 3849–3860.

Fry, N. 1979. Random point distributions and strain measurement in rocks. *Tectonophysics* **60**, 89–105.

Geiser, P. A. 1988. The role of kinematics in the construction and analysis of geological cross-sections in deformed terranes. In: *Geometries and Mechanisms of Thrusting* (edited by Mitra, G. & Wojtal, S.) *Spec. Pap. geol. Soc. Am.* **222**, 47–76.

Geiser, P. A. & Engelder, T. 1983. The distribution of layer-parallel-shortening fabrics in the Appalachian foreland of New York and Pennsylvania: evidence for two non-coaxial phases of the Appalachian orogeny. In: *Contributions to the Tectonics and Geophysics of Mountain Chains* (edited by Hatcher, R. D., Jr, Williams, H. & Zietz, I.). *Mem. geol. Soc. Am.* **158**, 118–130.

Gendzwill, D. J. & Stauffer, M. R. 1981. Analysis of triaxial ellipsoids: their shapes, plane sections, and plane projections. *Math. Geol.* **13**, 135–152.

Groshong, R. H., Jr. 1972. Strain calculated from twinning in calcite. *Bull. geol. Soc. Am.* **83**, 2025–2038.

Groshong, R. H., Jr. 1974. Experimental test of the least-squares strain gage calculation using twinned calcite. *Bull. geol. Soc. Am.* **85**, 1855–1864.

Groshong, R. H., Jr. 1988. Low temperature deformation mechanisms and their interpretation. *Bull. geol. Soc. Am.* **100**, 1329–1360.

Groshong, R. H., Jr., Pfiffner, O. A. & Pringle, L. R. 1984a. Strain partitioning in the Helvetic thrust belt of eastern Switzerland from the leading edge to the internal zone. *J. Struct. Geol.* **6**, 5–18.

Groshong, R. H., Jr., Teufel, L. W. & Gasteiger, C. 1984b. Precision and accuracy of the calcite strain-gage technique. *Bull. geol. Soc. Am.* **95**, 357–363.

Harris, A. G., Harris, L. D. & Epstein, J. B. 1978. Oil and gas data from Paleozoic rocks in the Appalachian Basin: Maps for assessing hydrocarbon potential and thermal maturity (conodont color alteration isograds and overburden isopachs). *U.S. geol. Surv. Misc. Inv. Map* I-917-E.

Harris, L. D. 1979. Similarities between the thick-skinned Blue Ridge anticlinorium and the thin-skinned Powell Valley anticline. *Bull. geol. Soc. Am.* **90**, 525–539.

Harris, L. D., de Witt, W., Jr. & Bayer, K. C. 1982. Interpretive seismic profile along interstate I-64 from Valley and Ridge to the Coastal Plain in central Virginia. *U.S. geol. Surv. Chart* OC-123.

Kamb, B. 1959. Ice petrofabric observation. *J. geophys. Res.* **64**, 1891–1909.

Kilsdonk, B. & Wiltschko, D. V. 1988. Deformation mechanisms in the southeastern ramp region of the Pine Mountain Block, Tennessee. *Bull. geol. Soc. Am.* **100**, 653–664.

Kulander, B. R. & Dean, S. L. 1988. The North Mountain–Pulaski fault system and related thrust sheet structure. In: *Geometries and Mechanics of Thrusting* (edited by Mitra, G. & Wojtal, S.). *Spec. Pap. geol. Soc. Am.* **222**, 107–118.

Lisle, R. J. 1985. *Geological Strain Analysis: A Manual for the* R_f/ϕ *Method*. Pergamon Press, New York.

Marshak, S. & Engelder, T. 1985. Development of cleavage in limestone of a fold-thrust belt in eastern New York. *J. Struct. Geol.* **7**, 345–359.

Mitra, G. & Elliott, D. 1980. Deformation of basement in the Blue Ridge and the development of the South Mountain cleavage. In: *The Caledonides in the U.S.A.* (edited by Wones, D. R.). *Mem. Dept. Geol. Sci., Virginia Tech.* **2**, 307–311.

Mitra, S. 1987. Regional variations in deformation mechanisms and structural styles in the central Appalachian orogenic belt. *Bull. geol. Soc. Am.* **98**, 569–590.

Nadai, A. 1963. *Theory of Flow and Fracture of Solids*. McGraw-Hill, New York.

Nathenson, M. & Guffanti, M. 1988. Geothermal gradients in the coterminous United States. *J. geophys. Res.* **93**, 6437–6450.

Nickelsen, R. P. 1986. Cleavage duplexes in the Marcellus shale of the Appalachian foreland. *J. Struct. Geol.* **8**, 361–371.

Peach, C. J. & Lisle, R. J. 1979. A Fortran IV program for the analysis of tectonic strain using deformed elliptical markers. *Comput. & Geosci.* **5**, 325–344.

Pfiffner, O. A. & Ramsay, J. G. 1982. Constraints on geological strain rates: arguments from finite strain states of naturally deformed rocks. *J. geophys. Res.* **87**, 311–321.

Ramsay, J. G. 1967. *Folding and Fracturing of Rocks*. McGraw-Hill, New York.

Ramsay, J. G. & Huber, M. I. 1983. *The Techniques of Modern Structural Geology, Volume 1: Strain Analysis*. Academic Press, New York.

Ramsay, J. G. & Huber, M. I. 1987. *The Techniques of Modern Structural Geology, Volume 2: Folds and Fractures*. Academic Press, New York.

Rejebian, V. A., Harris, A. G. & Heubner, J. S. 1987. Conodont color and textural alteration: An index to regional metamorphism, contact metamorphism, and hydrothermal alteration. *Bull. geol. Soc. Am.* **99**, 471–479.

Reks, I. J. & Gray, D. R. 1983. Strain patterns and shortening in a folded thrust sheet: an example from the southern Appalachians. *Tectonophysics* **93**, 99–128.

Rutter, E. H. 1974. The influence of temperature, strain rate and interstititial water in the experimental deformation of calcite rocks. *Tectonophysics* **22**, 311–334.

Rutter, E. H. 1976. Kinetics of rock deformation by pressure solution. *Phil. Trans. R. Soc. Lond.* **A283**, 203–219.

Sanderson, D. J. 1982. Models of strain variation in nappes and thrust sheets: A review. *Tectonophysics* **88**, 201–233.

Schmid, S. M. 1982a. Laboratory experiments on rheology and deformation mechanisms in calcite rocks and their application to studies in the field. *Mitt. geol. Inst. E.T.H. Univ. Zurich.* **241**, 1–106.

Schmid, S. M. 1982b. Microfabric studies as indicators of deformation mechanics and flow laws operative in mountain building. In: *Mountain Building Processes* (edited by Hsu, K. J.). Academic Press, London, 95–110.

Schmid, S. M., Boland, J. N. & Paterson, M. S. 1977. Superplastic flow in fine-grained limestone. *Tectonophysics* **43**, 257–291.

Schmid, S. M., Panozo, R. & Bauer, S. 1987. Simple shear experiments on calcite rocks: rheology and microfabric. *J. Struct. Geol.* **9**, 747–778.

Schmid, S. M., Paterson, M. S. & Boland, J. N. 1980. High temperature flow and dynamic recrystallization in Carra marble. *Tectonophysics* **65**, 245–280.

Suppe, J. 1983. Geometry and kinematics of fault-bend folding. *Am. J. Sci.* **283**, 684–721.

Suppe, J. & Wittke, J. H. 1977. Abnormal pore-fluid pressures in relation to stratigraphy and structure in the active fold-and-thrust belt of northwestern Taiwan. *Petrol. Geol. Taiwan.* **14**, 11–24.

Tissot, B. P. & Welte, D. H. 1978. *Petroleum Formation and Occurrence*. Springer, New York.

Turner, F. J. 1953. Nature and dynamic interpretation of deformation lamellae in calcite of three marbles. *Am. J. Sci.* **251**, 276–298.

Williams, G. D. & Chapman, T. J. 1983. Strains developed in the hangingwalls of thrusts due to their slip/propagation rate: a dislocation model. *J. Struct. Geol.* **5**, 563–571.

Wiltschko, D. V. 1979. A mechanical model for thrust sheet deformation at a ramp. *J. geophys. Res.* **84**, 1091–1104.

Wiltschko, D. V. 1981. Thrust sheet deformation at a ramp: summary and extension of an earlier model. In: *Thrust and Nappe Tectonics (edited by McClay, K. R. & Price, N. J.). Spec. Publs. geol. Soc. Lond.* **9**, 55–64.

Wiltschko, D. V., Medwedeff, D. A. & Millson, H. E. 1985. Distribution and mechanisms of strain within rocks on the northwest ramp of Pine Mountain block, southern Appalachian foreland: A field test of theory. *Bull. geol. Soc. Am.* **96**, 426–435.

Woodward, N. B., Gray, D. R. & Spears, D. B. 1986. Including strain data in balanced cross-sections. *J. Struct. Geol.* **8**, 313–324.

APPENDIX 1

Table of finite strain data

Site	Strain method*	Constant volume ellipsoid X	Y	Z	Section†	Profile R	θ	Deformation association
B31	F	1.30	0.96	0.80	MA	1.34	63	IVG+
B33	R	1.15	1.03	0.85	MA	1.36	110	IVG
B42	R	1.12	1.08	0.83	MA	1.35	82	III
B43	F	1.22	0.98	0.84	MA	1.31	76	IVG+
B81	R	1.33	1.04	0.72	STSK	1.85	—	IVR
C21	R	1.10	1.04	0.88	HWFS	1.22	88	IVG+
C22	R	1.07	1.01	0.92	HWFS	1.15	90	IVG+
C23	R	1.07	1.01	0.92	HWFS	1.10	78	IVG+
C51	R	1.04	1.00	0.97	HWFS	1.05	66	III
C72	R	1.03	1.01	0.96	HWFS	1.07	85	III
E21	R	1.19	1.04	0.81	—	1.43	86	IVG+
G13	R	1.30	0.97	0.79	STS	1.59	37	IVR
H31	F	1.15	1.07	0.82	STS	1.15	57	IVG+
H52	R	1.11	1.05	0.86	STS	1.25	46	IVG+
H81	R	1.15	1.00	0.87	STS	1.32	40	IVG+
H83	F	1.17	1.00	0.86	STS	1.26	63	IVG
H84	R	1.08	0.98	0.95	STS	1.09	60	IVG
H91	F	1.21	0.94	0.87	HWFN	1.41	70	IVG+
M21	R	1.24	0.98	0.83	HWFN	1.40	66	IVG+
M24	R	1.10	1.01	0.90	HWFN	1.19	60	IVG
M25	R	1.09	1.05	0.88	—	1.17	90	IVG
M29	R	1.13	1.00	0.88	HWFN	1.11	84	IVG+
M31	F	1.22	0.95	0.86	HWFN	1.35	68	IVG+
M32	F	1.11	0.97	0.93	HWFN	1.18	62	III
M62	R	1.07	0.99	0.94	—	1.08	74	IVG+
M63	F	1.17	1.00	0.85	HWFN	1.32	71	IVG+
M64	R	1.15	1.04	0.84	—	1.31	70	IVG+
M65	R	1.42	1.03	0.69	—	1.98	60	IVR
M66	R	1.36	0.93	0.79	HWFN	1.53	71	IVR
M91	F	1.33	1.04	0.72	—	1.75	87	IVR
M92	F	1.28	0.95	0.82	—	1.42	69	IVG+
M93	R	1.18	1.09	0.78	—	1.38	65	IVG+
M94	R	1.23	0.99	0.82	HWFN	1.31	57	IVG+
N52	R	1.12	1.01	0.89	MA	1.25	115	IVG
N61	R	1.09	1.02	0.90	MA	1.45	110	IVG+
N62	R	1.12	0.99	0.90	MA	1.24	81	IVG+
N63	R	1.22	1.02	0.81	MA	1.45	110	IVG+
P21	R	1.19	0.95	0.89	HWFN	1.30	117	IVG+
P71	R	1.12	1.03	0.87	HWFN	1.25	90	IVG+
P72	R	1.09	0.98	0.94	HWFN	1.15	78	IVG+
S11	R	1.47	1.04	0.66	STSK	2.25	—	IVR
S12	R	1.07	0.99	0.94	HWFN	1.14	41	IVR
S13	R	1.22	1.03	0.79	STSK	1.54	—	IVR
S14	F	1.54	0.99	0.66	STSK	2.35	—	IVG+
S21	F	1.12	0.99	0.90	STS	1.22	76	IVG
S31	R	1.24	1.09	0.78	STS	1.65	43	IVR
S32	R	1.11	1.00	0.90	—	1.25	43	IVG+
S41	R	1.14	1.00	0.87	STS	1.24	55	IVG+
S42	F	1.18	0.99	0.86	STS	1.22	78	IVG+
S43	F	1.35	0.89	0.84	STS	1.41	41	IVG+
S44	R	1.06	0.98	0.95	HWFS	1.11	35	III
S51	R	1.19	0.92	0.92	STS	1.30	77	IVG
S65	R	1.71	1.10	0.53	STSK	3.20	—	IVR
S81	R	1.12	0.95	0.95	HWFS	1.05	60	III
S93	R	1.28	1.02	0.77	STS	1.37	62	IVR
T11	R	1.18	1.00	0.84	HWFN	1.17	85	IVG+
T12	R	1.46	0.97	0.71	HWFN	1.87	24	IVR
T21	F	1.36	1.08	0.68	HWFN	2.05	77	IVR
T22	F	1.60	0.92	0.68	HWFN	1.84	71	IVR
T25	R	1.13	1.02	0.87	HWFN	1.17	75	IVG+
T32	F	1.09	1.01	0.92	HWFS	1.23	51	IVG+
T34	F	1.13	0.97	0.91	—	1.20	59	IVG+
T50	F	1.15	1.01	0.86	—	1.19	27	IVG+
T51	R	1.18	1.03	0.83	STS	1.23	22	IVG+
T52	F	1.08	1.02	0.91	HWFS	1.17	75	IVG+
T66	R	1.22	0.96	0.85	HWFN	1.24	20	IVG+
T67	R	1.37	1.00	0.73	HWFN	1.66	60	IVR
T71	F	1.18	0.98	0.87	HWFN	1.22	49	IVG
T72	R	1.19	1.00	0.84	—	1.36	32	IVG+
T73	F	1.10	0.97	0.94	—	1.17	30	IVG+
W82	F	1.20	1.00	0.84	—	1.47	40	IVG+
W91	R	1.31	0.96	0.79	—	1.92	34	IVR

*R = R_f/ϕ shape analysis; F = Fry spatial analysis.
†HWFN = Hangingwall flat north cross-section; HWFS = hangingwall flat south cross-section; MA = Mayland anticline; STS = Staunton thrust sheet; STSK = Staunton thrust sheet klippe.

APPENDIX 2

Calcite twin strains

Site	Strain method*	e_1	e_2	e_3	Section†	Profile R	Profile θ	% NEV‡	±Error	Deformation association
B33	CSG	3.00	0.40	−3.40	MA	1.07	72	17	0.40	IVG
B42	CSG	2.40	0.30	−2.60	MA	1.05	110	25	0.41	III
B51	CSG	11.00	−4.10	−6.90	MA	1.19	55	18	0.84	IVG
C72	CSG	3.20	−1.30	−1.90	HWFS	1.05	36	24	0.50	IVG
H31	CSG	3.60	1.20	−4.80	STS	1.09	42	18	0.54	IVG+
H81	CSG	1.10	0.30	−1.30	STS	1.02	40	29	0.31	IVG+
H84	CSG	2.00	−0.50	−1.50	STS	1.04	36	29	0.36	IV
M31	CSG	3.60	1.20	−4.80	HWFN	1.09	80	8	0.54	IVG+
M71	CSG	2.50	−0.30	−2.20	HWFN	1.05	90	8	0.19	III
N51	CSG	4.20	0.30	−4.50	MA	1.09	98	30	1.03	IVG
P71	CSG	4.50	0.30	−4.80	—	1.10	90	33	0.72	IVG+
S12	CSG	4.60	−1.60	−3.00	HWFN	1.08	30	13	0.58	III
S44	CSG	1.30	0.30	−1.50	HWFS	1.03	58	20	0.26	III
T13	CSG	1.40	−0.30	−1.10	MA	1.03	104	32	0.42	III
T14	CSG	2.40	−0.60	−1.90	MA	1.04	105	18	0.18	III
T31	CSG	2.30	0.30	−2.60	HWFN	1.05	68	29	0.35	III
T51	CSG	7.30	0.90	−8.10	STS	1.17	14	26	0.96	IVG+
T64	CSG	3.00	0.30	−3.20	HWFN	1.06	30	41	1.16	IVG+
W92	CSG	3.50	−0.10	−3.40	HWFN	1.07	77	13	0.43	III

* CSG = calcite strain gauge technique.
† Abbreviations as in Appendix 1.
‡ % NEV = % negative expected value.